GMP-selected dual and lensed AGNs: selection function and classification based on near-IR colors and resolved spectra from VLT/ERIS, Keck/OSIRIS, and LBT/LUCI

Mannucci, F.; Scialpi, M.; Ciurlo, A.; Yeh, S.; Marconcini, C.; Tozzi, G.; ... ; Kenworthy, M.A.

A&A 680, A53 (2023)
https://doi.org/10.1051/0004-6361/202346894

Astronomy & Astrophysics

GMP-selected dual and lensed AGNs: Selection function and classification based on near-IR colors and resolved spectra from VLT/ERIS, Keck/OSIRIS, and LBT/LUCI

F. Mannucci[1], M. Scialpi[4,1], A. Ciurlo[2], S. Yeh[3], C. Marconcini[4,1], G. Tozzi[4,1], G. Cresci[1], A. Marconi[4,1], A. Amiri[5,4], F. Belfiore[1], S. Carniani[6], C. Cicone[7], E. Nardini[1], E. Pancino[1], K. Rubinur[7], P. Severgnini[8], L. Ulivi[4,1], G. Venturi[6,1], C. Vignali[9], M. Volonteri[10], E. Pinna[1], F. Rossi[1], A. Puglisi[1], G. Agapito[1], C. Plantet[1], E. Ghose[1], L. Carbonaro[1], M. Xompero[1], P. Grani[1], S. Esposito[1], J. Power[11], J. C. Guerra Ramon[11], M. Lefebvre[11], A. Cavallaro[11], R. Davies[12], A. Riccardi[1], M. Macintosh[13], W. Taylor[13], M. Dolci[14], A. Baruffolo[15], H. Feuchtgruber[12], K. Kravchenko[12], C. Rau[12], E. Sturm[12], E. Wiezorrek[12], Y. Dallilar[12,16], and M. Kenworthy[17]

[1] INAF – Osservatorio Astrofisico di Arcetri, Largo E. Fermi 5, 50125 Firenze, Italy
e-mail: filippo.mannucci@inaf.it
[2] Department of Physics and Astronomy, University of California Los Angeles, 430 Portola Plaza, Los Angeles, CA 90095, USA
[3] W. M. Keck Observatory, 65-1120 Mamalahoa Highway, Kamuela, HI 96743, USA
[4] Dipartimento di Fisica e Astronomia, Università di Firenze, Via G. Sansone 1, 50019 Sesto Fiorentino, Firenze, Italy
[5] Department of Physics, University of Arkansas, 226 Physics Building, 825 West Dickson Street, Fayetteville, AR 72701, USA
[6] Scuola Normale Superiore, Piazza dei Cavalieri 7, 56126 Pisa, Italy
[7] Institute of Theoretical Astrophysics, University of Oslo, PO Box 1029, Blindern 0315, Oslo, Norway
[8] INAF – Osservatorio Astronomico di Brera, Via Brera 28, 20121 Milano, Italy
[9] Physics and Astronomy Department "Augusto Righi", Università di Bologna, Via Gobetti 93/2, 40129 Bologna, Italy
[10] Institut d'Astrophysique de Paris, 98bis Bd Arago, 75014 Paris, France
[11] Large Binocular Telescope Observatory, Tucson, AZ, USA
[12] Max-Planck-Institut für Extraterrestrische Physik, Postfach 1312, 85741 Garching, Germany
[13] STFC UK ATC, Royal Observatory Edinburgh, Blackford Hill, Edinburgh EH9 3HJ, UK
[14] INAF – Osservatorio Astronomico d'Abruzzo, Via Mentore Maggini, 64100 Teramo, Italy
[15] INAF – Osservatorio Astronomico di Padova, Vicolo dell'Osservatorio 5, 35122 Padova, Italy
[16] I. Physikalisches Institut, Universität zu Köln, Zülpicher Str. 77, 50937 Köln, Germany
[17] Leiden Observatory, University of Leiden, PO Box 9513, 2300 RA Leiden, The Netherlands

Received 13 May 2023 / Accepted 9 October 2023

ABSTRACT

The *Gaia* Multipeak (GMP) technique can be used to identify large numbers of dual or lensed active galactic nucleus (AGN) candidates at subarcsec separation, allowing us to study both multiple supermassive black holes (SMBHs) in the same galaxy and rare, compact lensed systems. The observed samples can be used to test the predictions of the models of SMBH merging when (1) the selection function of the GMP technique is known, and (2) each system has been classified as a dual AGN, a lensed AGN, or an AGN/star alignment. Here we show that the GMP selection is very efficient for separations above 0.15″ when the secondary (fainter) object has a magnitude $G \lesssim 20.5$. We present the spectroscopic classification of five GMP candidates using VLT/ERIS and Keck/OSIRIS and compare them with the classifications obtained from (a) the near-IR colors of seven systems obtained with LBT/LUCI, and (b) the analysis of the total spatially unresolved spectra. We conclude that colors and integrated spectra can already provide reliable classifications of many systems. Finally, we summarize the confirmed dual AGNs at $z > 0.5$ selected by the GMP technique, and compare this sample with other such systems from the literature, concluding that GMP can provide a large number of confirmed dual AGNs at separations below 7 kpc.

Key words. quasars: emission lines – quasars: general

1. Introduction

The existence of dual AGNs, that is, pairs of active supermassive black holes (SMBH) at kiloparsec separations that are inspiralling in the same galaxy, is one of the fundamental predictions of current models of galaxy and SMBH formation and evolution (e.g. Tremmel et al. 2017). The study of these systems allows us to test the formation and evolution models of binary SMBHs. These systems are particular important because mergers of SMBHs in the mass range 10^4–$10^9\,M_\odot$ will dominate the gravitational wave (GW) events detected by the future Laser Interferometer Space Antenna (LISA) space mission and by the Pulsar Timing Arrays (e.g., Arzoumanian et al. 2018; Amaro-Seoane et al. 2023). Dual AGNs allow us to investigate the starting conditions of the merging process and to interpret future GW results (e.g. DeGraf et al. 2023; Dong-Páez et al. 2023; Chen et al. 2023a).

Models of galaxy and SMBH coevolution predict that dual AGNs at small separations (smaller than 10 kpc) are quite common and make up even a few percent of all existing AGNs at

$z > 0.5$, where the merging activity is expected to be stronger than in the local Universe (Volonteri et al. 2022). Dual AGNs therefore must exist in a significant fraction of galaxies. Despite these expectations and a decade of active searches, only a handful of confirmed dual AGNs at small separations are currently known (see Chen 2021, for a recent compilation of the existing data).

These objects can only be detected through imaging with a spatial resolution that is considerably better than one arcsecond. They typically require observation from space (see De Rosa et al. 2019, for review). Because they are rare systems, they also require very wide field surveys. The ESA mission *Gaia* (Gaia Collaboration 2016) is currently the only mission providing high-resolution data over large areas of the sky. It can therefore be exploited to detect dual and lensed AGNs. The presence of multiple *Gaia* sources that are associated within a few arcseconds to known AGNs (the "multiplicity" method) has been used by several authors (e.g. Lemon et al. 2018; Chen et al. 2022) to detect both dual and lensed systems. The additional astrometric jitter induced by AGN variation in unresolved pairs was also exploited to select several multiple AGN candidates (e.g. Shen et al. 2019; Hwang et al. 2020; Chen et al. 2022).

Recently, in Mannucci et al. (2022), we developed the GMP method, which exploits the *Gaia* catalog to select a large number of dual AGN candidates at subarcsecond separations. This method is based on the detection of multiple peaks in the light profiles of otherwise unresolved AGNs. Using spatially resolved imaging and spectroscopy, we showed that the GMP is a very effective method for selecting dual systems, while in Ciurlo et al. (2023) and Scialpi et al. (2023), we built the first sample of spectroscopically confirmed GMP-selected dual AGNs at subarcsecond separations.

The GMP technique is expected to provide a large number of confirmed dual AGNs, especially at $z > 0.3$, where the host galaxy does not contribute significantly to the *Gaia* light profile. These results will be compared with the expectations from the models of galaxy and SMBH formation and coevolution, which predict various quantities such as the distribution in separation, luminosity and mass ratio, or redshift (Steinborn et al. 2016; Capelo et al. 2017; Rosas-Guevara et al. 2019; Volonteri et al. 2022; Chen et al. 2023a). The samples of GMP-selected dual AGNs will provide strong constraints on these models when the efficiency of this method in selecting multiple systems is known as a function of separation and luminosity of the components.

The quasi-stellar objects (QSOs) showing multiple components need to be classified as either a pair of AGNs (either a dual system or a single AGN that is lensed by a foreground galaxy) or an alignment between an AGN and a foreground star. Different possibilities exist. First, the classification is usually obtained by spatially resolved spectroscopy from space (e.g. Junkkarinen et al. 2001; Mannucci et al. 2022) or by adaptive-optics (AO) assisted spectroscopy from the ground (e.g. Ciurlo et al. 2023; Scialpi et al. 2023). The resulting classification can be very reliable, but obtaining resolved spectroscopy is very expensive in telescope time and limits the number of confirmed systems. Second, spatially unresolved spectroscopy, usually from the ground in seeing-limited conditions, can be analyzed to detect stellar features at zero velocity, revealing the presence of a star projected close to the AGN (Shen et al. 2023; Scialpi et al. 2023). These data cannot distinguish dual and lensed systems because the spectral differences are not expected to be large enough to be seen in the total spectrum in both cases. Third, because stars and AGNs in most cases have different colors, multiband spatially resolved imaging can be used to study the nature of the two components (e.g. Chen et al. 2022; Chen 2021). Intrinsic luminosities can also be used to identify lensed systems, which in many cases are much brighter than the typical AGN at the same redshift.

By applying these three different classification methods to the same targets, we show in this paper that spatially resolved imaging and spatially unresolved spectroscopy can complement resolved spectroscopy in classifying at least part of the systems: we can distinguish between dual AGNs, lensed systems, and star/AGN alignments.

In Sect. 2 we discuss the statistical properties of the GMP-selected systems in terms of luminosity ratios and projected separation. In Sect. 3 we present and compare the different classification techniques. In Sect. 3.1 we describe the Large Binocular Telescope (LBT) observations of seven targets aimed at measuring the near-IR colors of each component. Section 3.2 describes that the analysis of the integrated spectra can reveal stars that are projected close to the AGN. In Sect. 3.3 we present spatially resolved ESO Very Large Telescope (VLT) and Keck spectra of five GMP-selected targets, which include two confirmed dual AGNs and one compact lensed system. In Sect. 3.4 we compare the results of the three classifications. Finally, in Sect. 4, we summarize the state of GMP target observations and discuss the results in the broader context of observed dual AGNs at small separations.

2. GMP selection efficiency and contamination

The GMP technique is based on the detection of multiple peaks in the light profiles of known AGNs in the multiple *Gaia* scans. The *Gaia* DR3 catalog (Gaia Collaboration 2023) provides the parameter ipd_frac_multi_peak (`FMP`), which contains the percent fraction of scans showing a multiple peak for a given target. The value of this parameter, which ranges from 0 (multiple peak never detected) to 100 (always detected), is determined by several factors. Separation and luminosity ratios are important parameters to consider because pairs whose separations are too small and/or whose luminosity ratios are too high will not produce a measurable double peak. Because *Gaia* obtains sky scans in multiple directions, an object pair will not show a double peak when the scanning direction is perpendicular to the separation line. In addition, when scanning objects with separations δ larger than or of about the *Gaia* photometric window (0.7″, Gaia Collaboration 2016), the components may be separated into different catalog entries, each one with a single peak and a low value of `FMP`. In contrast, because *Gaia* projects on the same array two different fields 106.5° apart (Gaia Collaboration 2016), double peaks can occasionally be detected in the light profile of isolated objects because they are aligned with a source in the other field. Thus, the selection requires a statistical approach and needs to meet the following complementary challenges: First, define the minimum value of `FMP` to keep the level of contamination by false positives (single systems with values of `FMP` above threshold) low; second, easure the efficiency of the GMP method of detecting multiple objects as a function of magnitudes and angular separations δ of the components.

These two problems can be addressed by testing the values of `FMP` that are obtained by apparent stellar pairs in moderately crowded stellar fields as a function of their magnitude and separations. To do this, we used the stellar catalogs[1] of 110 parallel

[1] http://groups.dfa.unipd.it/ESPG/hstphot.html

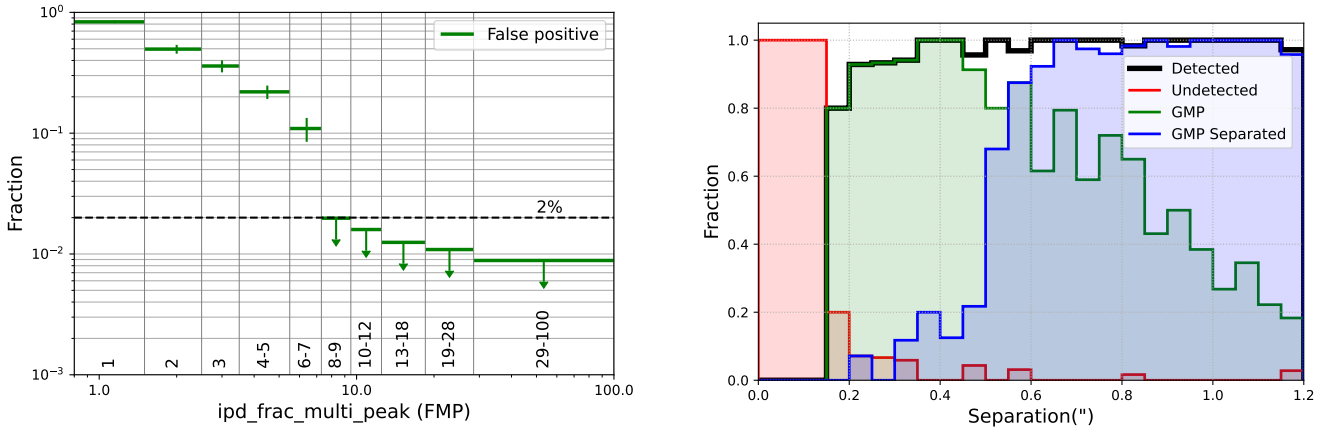

Fig. 1. Statistical properties of the GMP selection. Left: level of contamination of false positives (objects with a detection of multiple peaks that are not projected pairs) as a function of the FMP values in a sample of dense stellar fields for $G < 20.5$. No false positives are found for FMP ≥ 8, where we plot 90% upper limits, i.e., the levels that would correspond to 2.3 false positives. Right: fraction of recovered projected pairs as a function of separation (δ) in arcseconds. The red histogram shows the pairs that are not recovered, which dominate the counts at $\delta < 0.15''$ and are very rare at $\delta > 0.20''$. The green histogram reports the fraction of recovered isolated objects that correspond to single entries in the *Gaia* source catalog, and the blue histogram shows the GMP-selected objects that have nearby companions in the catalog. The combination of these two GMP populations is show by the black line.

fields observed with HST/ACS[2] in the $F475W$ and $F814W$ filters in the outskirts of 48 globular clusters (GCs) by Piotto et al. (2015) and Simioni et al. (2018). The depths and spatial resolutions of these images are better than those in *Gaia*, and as a consequence, they can be used to obtain a sample of projected pairs and to test the performance of the GMP method. Even when the central parts of the GCs are avoided, some of these fields are very crowded. We limited our analysis to the 84 fields in which the densities are such that the average distance of a source to the closest object is larger than $5''$. Higher densities tend to have too many objects at close projected distances. This regime is absent in the high galactic latitude fields that are used for the GMP selection, and they could affect *Gaia* detection properties. A restriction to lower densities would result in a low number of projected pairs at low separation. Regions within $5''$ of bright stars ($G < 15.5$) were excluded because the rectangular *Gaia* primary mirrors produce long diffraction spikes that could produce the detection of secondary peaks in nearby sources.

2.1. Contamination

The level of contamination by false positives, that is, objects with high values of FMP that are not projected pairs at the HST/ACS resolution (~$0.05''$), can be estimated by considering all the objects in the observed fields whose FMP is above a given threshold in the *Gaia* catalog and by investigating the fraction that does not correspond to pairs in the HST catalog. The results are shown in the left panel of Fig. 1. While at FMP = 1 the fraction of false positives is about 80%, no false positives are found with FMP ≥ 8 far from bright stars. The maximum fraction of false positives is at the percent level in each of the bins with FMP ≥ 8 shown in Fig. 1, and it is below $\sim 2 \times 10^{-3}$ considering all of them together.

2.2. Efficiency

The efficiency of the pair detection can be estimated by the ratio of the number of recovered pairs versus the total number of pairs present in the HST data as a function of magnitude and separation δ. Our catalog contains about 1300 projected pairs with $\delta < 1.2''$ and with a primary of $G < 21$ mag. The fraction of recovered objects (FMP > 8) with $G < 20.5$ mag as a function of separation is shown in the right panel of Fig. 1. The pairs that are not recovered (red histogram) dominate the counts at $\delta < 0.15''$. Above this limit, virtually all the projected pairs are recovered within our magnitude limit. GMP objects that are isolated in the *Gaia* catalog, that is, without another object within $1.5''$, are shown in green. Systems that correspond to two nearby entries in the catalog and that therefore can also be identified without the use of the GMP method are shown in blue. The isolated population dominates separations between $0.15''$ and $0.6''$, while above this limit, most of the objects are separated in the catalog. The separated population can also be identified by simply looking for pairs of objects at close separations in the *Gaia* archive, without considering the FMP parameter. In particular, this population becomes dominant at $\delta > 0.6''$, while below this limit, most of the targets are isolated and can only be recovered with the GMP method.

For $G < 20.5$ mag and $\delta > 0.15''$, the selection efficiency does not critically depend on magnitude and separation. This is shown in Fig. 2, where we plot the efficiency as a function of both primary and secondary magnitudes at different separations. The estimate of the G-band magnitude of the secondary stars that are undetected by *Gaia* was derived from the photometry in the HST $F814W$ band by applying a color correction derived from the detected sources. Provided that the fainter object has $G < 20.5$ mag and the separation is $\delta > 0.15''$, the efficiency is high and not strongly dependent on these parameters. This is a critical point that will allow us to compare the observational results with the models. Figure 2 also shows that if the primary component has $G > 17$ mag, the GMP method can efficiently select systems with a secondary as faint as $G = 20.5$ mag. The range of brighter magnitudes, $G < 17$ mag, is not sampled in our fields, but it is not very relevant because the majority of AGNs at $z > 0.5$ are fainter than this limit. As a consequence, the range of the luminosity ratio that is sampled with the GMP method depends on the luminosity of the primary source. For $G = 18.5$ mag, a typical value for bright AGN at $z > 1$, the magnitude difference with the secondary member is limited to

[2] *Hubble* Space Telescope, Advanced Camera for Surveys.

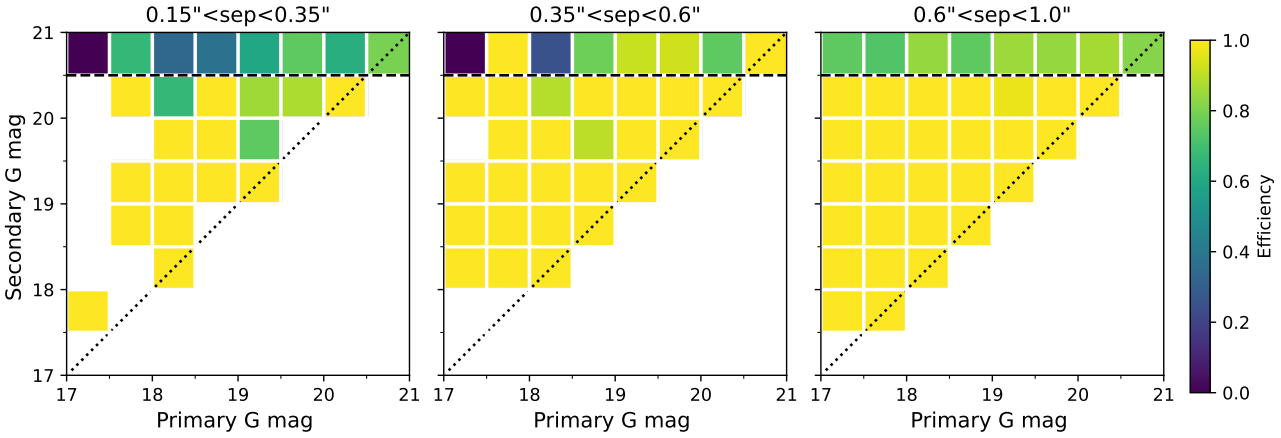

Fig. 2. Efficiency of the GMP method as a function of G mag of the primary and primary and secondary components in three separation ranges. The efficiency does not show strong dependences on the three parameters up to secondary G magnitudes of 20.5. This is shown by the dashed line.

Table 1. Main properties of the targets used to compare the various techniques and source of the observational data.

Target	RA	Dec	z	FMP	G [(a)]	Integ. spectrum [(b)]	Resolved colors	Resolved spectra
J0732+3533	07:32:51.57	+35:33:15.3	3.065	10	20.31	DR16	LBT/LUCI	–
J0812–0040	08:12:19.34	–00:40:47.9	1.912	20	20.36	DR16	LBT/LUCI	–
J0812+2007	08:12:46.41	+20:07:30.1	1.48	23	20.16/20.44	DR16	LBT/LUCI	Keck/OSIRIS
J0927+3512	09:27:48.42	+35:12:41.3	1.149	49	15.86	LAMOST	LBT/LUCI	–
J0950+4329	09:50:31.63	+43:29:08.6	1.770	78	17.90	DR16	LBT/LUCI	Keck/OSIRIS
J1048+4541	10:48:20.91	+45:41:41.3	1.441	13	20.02	DR16	–	Keck/OSIRIS
J1103+2348	11:03:08.10	+23:48:05.8	1.441	17	20.16	DR16	–	Keck/OSIRIS
J1318–0136	13:18:58.73	–01:36:42.5	1.486	17	20.03	2QZ	LBT/LUCI	VLT/ERIS
J1510+5959	15:10:45.51	+59:59:19.0	2.004	34	20.34	DR16	LBT/LUCI	–

Notes. [(a)]Total *Gaia* G-band magnitude, with the exception of J0812+2007, which is separated into two targets in the *Gaia* catalog, and for which we report the magnitude of both objects. [(b)]Integrated spectra from SDSS DR16 (Lyke et al. 2020), LAMOST (Yao et al. 2019), and 2QZ (Croom et al. 2004).

~2 mag, a factor of ~6 in luminosity. This limits the number of detected sources, but guarantees that both components contribute to some extent to the integrated spectra, as discussed in the next section. Higher luminosity ratios can be covered with the ESA satellite *Euclid* (Euclid Collaboration 2022). Multiple AGN detections with *Euclid* will be discussed in a future paper (Ulivi et al., in prep.).

3. Classifying multiple systems in different ways

Because the GMP technique only provides evidence of the presence of multiple components in an AGN, the classification of these components requires additional observations. As shown in Mannucci et al. (2022), Ciurlo et al. (2023), and Scialpi et al. (2023), resolved spectroscopy is the ultimate technique, but is very demanding observationally and requires a high spatial resolution. For this reason, we investigate in this section how spatially resolved colors (Sect. 3.1) and total spectra (Sect. 3.2) can provide a classification of the components. To do this, we considered a sample of nine GMP-selected systems (see Table 1) with archival total spectra. We obtained spatially resolved colors of seven of them with the LBT Utility Camera in the Infrared one (LUCI1) at LBT, and spatially resolved spectra of five of these systems with the Keck OH-Suppressing Infra-Red Imaging Spectrograph (OSIRIS) and the Enhanced Resolution Imager and Spectrograph (ERIS) on VLT. The target selection is described in Sects. 3.1.1 and 3.3 for the LBT and Keck+VLT samples, respectively. The classifications based on these three data sets are compared in Sect. 3.4.

3.1. Classification using near-IR colors

3.1.1. LBT imaging

We obtained AO-assisted imaging of seven GMP-selected systems at the LBT, including the five multiple systems presented in Mannucci et al. (2022). We extracted the targets from the Milliquas catalog v7.2 (Flesch 2021), selecting objects with secure AGN classification and redshifts, and within ~30″ of suitable natural-guide stars (NGS) to drive the AO system. After cross-correlating with the *Gaia* archive, we selected systems with FMP ≥ 10, a more conservative limit that the value FMP ≥ 8 defined in Sect. 2. Six out of seven targets are isolated, that is, have no companion in the *Gaia* catalog, while J0812+2007 has a known companion that lies 0.66″ away.

Observations were performed on March 9, 2022, for objects J0732+3533, J0812–0040, J0812+2007, J0927+3512, and J0950+432, and on June 3, 2022, for J1318–0136 and J1510+5959. We used the imager and spectrograph (Mandel et al. 2007) with the bf single conjugate AO update (SOUL) AO module (Pinna et al. 2016, 2021). Each system was observed in the near-IR H and K_s filters with integration times of

Table 2. Main properties of the targets observed with LBT.

Target	Sep. (″)	Primary		Secondary	
		(H mag)	(K_s mag)	(H mag)	(K_s mag)
J0732+3533	0.52	18.02±0.05	17.69±0.05	18.63±0.05	18.13±0.05
J0812–0040	0.66	19.58±0.05	19.58±0.05	20.32±0.05	19.64±0.05
J0812+2007	0.54	19.57±0.30	18.56±0.05	19.63±0.30	19.21±0.05
J0927+3512	0.33	14.40±0.05	14.42±0.05	15.38±0.05	15.30±0.05
J0950+4329	0.37	14.98±0.05	14.34±0.05	15.47±0.05	14.98±0.05
J1318–0136	0.27	18.83±0.20	18.62±0.10	18.94±0.20	18.61±0.10
J1510+5959	0.28	19.57±0.15	19.27±0.10	20.20±0.15	19.46±0.10

6 min in H and 24 min in K_s in the March run and 15 min each in H and K_s for the June run. In all cases, we used an image sampling of 15 mas pix^{-1}. Data reduction was performed with our custom-made Python reduction routine (PySnap). The seeing was rather variable during the June 2022 run, and we automatically rejected single images showing a point-spread function (PSF) that was significantly worse than the average.

All the systems show two components at subarcsecond separation. The K_s-band imaging of these sources was presented in Mannucci et al. (2022). In Table 2 we summarize the observed magnitudes and the main properties of the observed objects. All the sources are well resolved in the H and K_s bands, except for J0812+2007 in the H band (see below). This image was obtained under poor seeing conditions, and the resulting PSF (full width at half maximum $FWHM \sim 0.65''$) is even larger than the separation (0.54″). As a consequence, the relative photometry of the two components (see below) in this band is unreliable.

Photometry was performed by PSF fitting. Because the two sources in each system lie at very short distance to each other, they are expected to have the same PSF. We thus fit two elliptical Gaussian functions with the same shape (FWHM and position angle), centers defined on the image with the best resolution, and free normalization. This procedure provides reliable values of the parameters even when the PSF FWHM is not significantly smaller than the separation and the sources are not well resolved. Because two systems are bright enough to be in the Two Micron All Sky Survey (2MASS) catalog (Skrutskie et al. 2006), we used their total magnitudes to obtain an absolute flux calibration. In all cases in which the sources are well resolved, the uncertainties are dominated by flux calibrations, estimated to be $\Delta(\mathrm{mag}) \sim 0.05$. J1318–0136, and J1510+5959 are the two most compact systems, with separations of 0.27″ and 0.28″, similar to the PSF FWHM. In these cases, we estimate larger photometric errors of 0.10 and 0.15 mag. For the H-band photometry of J0812+2007 with the poor seeing, we estimate that the errors on the relative photometry are $\Delta(\mathrm{mag}) \sim 0.30$.

3.1.2. Spatially resolved colors

Figure 3 shows the color-magnitude diagram for each component of the systems of the LBT sample, compared with QSOs and stars from the literature. For the QSOs, we used the 2MASS magnitudes of the Sloan Digital Sky Survey (SDSS) DR16Q quasar catalog[3] (Lyke et al. 2020), and the much fainter QSOs in Cosmic Evolution Survey (COSMOS) by Civano et al. (2016)[4]. These two catalogs probe the entire luminosity range covered by the current sample ($15 < H < 21$). For the stars at high Galactic latitudes, we used the observed magnitudes of a star sample from the SDSS, and the model magnitudes of stars from the Tridimensional model of the Galaxy (TRILEGAL; Girardi et al. 2005; Vanhollebeke et al. 2009). The stars show relatively blue $H - K_s$ colors of about 0.0–0.2, while QSOs span a wider range and mostly have redder colors $0.4 < H - K_s < 1.2$ that evolve little with magnitude (and therefore redshift).

The observed colors may be affected by dust in the AGN or in its host galaxy, whose effect depends not only on its column density, but also on the redshift of the QSO because our images sample progressively bluer wavelengths at higher redshift. As a reference, Fig. 3 shows the extinction arrows for $A_V = 1$ for three different values of redshift.

The 14 components of the seven LBT systems span a large part of this diagram. Information about the nature of each component can be derived from its position in this color-magnitude diagram, that is, by comparing it with the distribution of stars and QSOs. A very small fraction of stars with a high Galactic latitude have colors $H - Ks \gtrsim 0.35$, which shows that these objects with significantly redder colors can be identified as QSOs, while objects with bluer colors are most likely stars. For all systems except for J0812+2007, we do not know which dominates the optical spectrum and thus causes the classification as a QSO.

One component of J0812–0040, J1318–0136, and J1510+5959 (systems 2, 6, and 7 in Fig. 3) shows combinations of very blue colors and H-band magnitudes that are consistent with stars, while the other component has red $H - K_s$ colors that are typical of AGNs. These systems are therefore better described by AGN/star alignments. These occurrences are expected to be present in our sample at the 30% level for separations larger than 0.5″ (Mannucci et al. 2022). It is very unlikely but not entirely impossible that these systems are constituted by two AGNs.

One component of J0732+3533 and J0812+2007 (systems 1 and 3) is compatible with being an AGN, and the other component is consistent with both AGNs and stars. As a consequence, the colors cannot provide a classification of these two objects.

The colors of the two components of J0950+4329 (system 5) are only compatible with QSOs, and therefore, this is either a dual or a lensed AGN. This is a very bright object at $z = 1.77$ and lies at the upper luminosity envelope of the bright QSOs at this distance in Croom et al. (2009). It is also several magnitudes brighter than the typical COSMOS QSOs at that redshift (Civano et al. 2016). For this reason, J0950+4329 is most likely a lensed AGN whose luminosity is boosted by lensing magnification. The slightly different observed $H - K_s$ colors of the two components could be due to different degrees of

[3] https://www.sdss.org/dr16/algorithms/qso_catalog/
[4] https://cdsarc.cds.unistra.fr/viz-bin/cat/J/ApJ/819/62

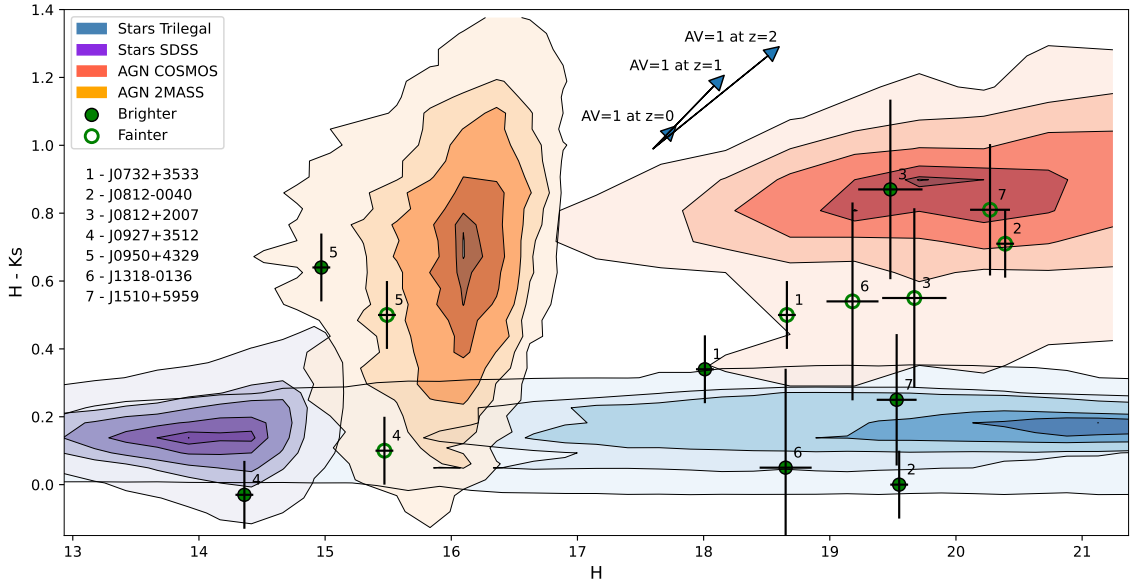

Fig. 3. Near-IR colors and magnitudes of the observed targets. The blue and purple contour plots show the distribution of Galactic stars from the TRILEGAL model (Girardi et al. 2005) and from the SDSS, respectively, while orange and red contours show AGNs from SDSS DR16Q (Lyke et al. 2020) and COSMOS (Civano et al. 2016), respectively.

extinction in the lensing galaxy. Based on the separation and the redshift of the system, the lensing galaxy is expected to have $H \sim 19-20$ and therefore would be outshone by the lensed QSOs.

Finally, the two components of J0927+3512 (system 4) show very blue $H - K_s$ colors; the brighter component is only compatible with being a star, but the fainter component could be either a star or a very bright (for its tabulated redshift of 1.149) and very blue AGN. The magnitude and colors of this system are more compatible with being a double star, despite its classification as an AGN based on a spectrum from the Large Sky Area Multi-Object Fiber Spectroscopic Telescope (LAMOST) survey. This point is further discussed in Sect. 3.2.

Objects fully resolved by *Gaia*, that is, with a value of the G magnitude for each component, can also be classified in a color-color plane involving both optical and near-IR magnitudes. This would offer the advantage of sampling a larger wavelength range and would provide a better classification of any companion star. In our sample, only J0812+2007 belongs to these resolved targets, but the large error of its H-band magnitude prevents us from deriving any additional useful information.

In Sect. 3.4 these classification based on resolved colors are compared with those obtained from the total and spatially resolved spectroscopy derived in the next sections.

3.2. Classification using unresolved spectroscopy

Ground-based spectra are primarily used to discover AGNs and measure their redshifts. Most of the available QSO spectra come from the SDSS DR16Q (Lyke et al. 2020), 2dF QSO Redshift Survey (2QZ; Croom et al. 2004), and LAMOST (Yao et al. 2019) surveys. As shown in Sect. 2, in GMP-selected systems the luminosity ratio of the primary and the secondary object is usually not high, and it is below a factor of six for all objects with $G > 18.5$. For this reason, ground-based spectra, which are usually blend of all the components, can also be used to identify the systems containing a star if they can be reproduced with the superposition of an AGN and a star.

Following the procedure described in Scialpi et al. (2023), we deconvolved the spectra of all the targets in Table 1. The observed spectra were fit with a combination of an AGN (Vanden Berk et al. 2001; Temple et al. 2021) and a stellar template (Covey et al. 2007). The fitting parameters, determined with a χ^2 minimization, are the normalization of the two spectra, the redshift of the AGN, the radial velocity of the star (limited to $\pm 300\,\mathrm{km\,s^{-1}}$), and the level of dust extinction of the AGN template. LBT observations were obtained without performing any spectroscopic analysis, thus the LBT sample is unbiased toward systems constituted by two AGNs (either dual or lensed) and AGN/star associations. In contrast, Keck observations were targeted toward systems without clear stellar features in the blended ground-based spectra, except for J0812+2007, which was observed because it was already included in the LBT sample. The ERIS target J1318−0136 was also observed because it was part of the LBT sample.

The results of the deconvolution for the objects in Table 1 are reported in Table 5 and are plotted in the appendix. They show that

- J0732+3533, J0950+4329, J1048+4541, and J1103+2348 can be fit well by a single-AGN spectrum and do not show any stellar feature.
- In contrast, J0812+2007, J0812-0040, and J1510+5959 show clear stellar features that reveal a projected star.
- J1318−0136 has an uncalibrated spectrum with a low S/N from the 2QZ survey (Croom et al. 2004), with problematic features. Our estimate of the redshift is based on the line at ∼3850 Å, which wa identified as CIVλ1549 based on two low-significance features at 4800 Åand 6950 Å, which might be identified as CIII and MgII. Even if our estimate agrees with that originally provided by 2QZ, the redshift determination is not certain. Moreover, the quality of the spectrum does not allow us to search for stellar features, and therefore, this total spectrum does not provide any classification.
- J0927+3512 is a peculiar object. It was observed by LAMOST and classified as a QSO at $z = 1.149$ based on a broad feature at 4050 Å. Nevertheless, this feature has a low S/N,

Table 3. Properties of the targets observed with OSIRIS/Keck and ERIS/VLT, together with the observational setup.

Target	Instrument	Band [(a)]	T_{exp} (min)	$FWHM$ ($''$) [(b)]
J0812+2007	OSIRIS	Hbb	60	0.11
J0950+4329	OSIRIS	Jbb	30	0.15
J1048+4541	OSIRIS	Hn3	45	0.14
J1103+2348	OSIRIS	Hn3	75	0.17
J1318–0136	ERIS	Hlow	40	0.12

Notes. [(a)]Observed band reported as in the instrument user manuals. [(b)]FWHM of the PSF, calculated on isolated sources.

and no other convincing emission line is present. Moreover, the MgII line expected at ∼6000 Å for this redshift is absent, and the continuum shape shows a peculiar shape, with a minimum in F_λ around 7500 Å. This spectrum does not convincingly show that an AGN is present in this system at all. Therefore, J0927+3512 remains unclassified.

3.3. Classification using resolved spectroscopy

We observed four GMP-selected systems with the integral-field spectrograph (IFS) OSIRIS on the Keck telescope and one target with ERIS/SPIFFIER on the VLT. In both cases, the use of laser-assisted AO allowed us to fully resolve the systems and obtain independent spectra for the two components. These sources were selected to have $\texttt{FMP} \geq 10$, which is a more conservative value than the minimum $\texttt{FMP} = 8$ derived in Sect. 2. We extracted the targets from the Milliquas v7.9 catalog (Flesch 2021), considering known AGNs with a spectroscopic redshift so that either Hα or Hβ were placed inside one of the available near-IR bands ($0.85 < z < 1.11$, $1.28 < z < 1.85$, and $2.03 < z < 2.65$ for OSIRIS; $0.70 < z < 1.02$, $1.27 < z < 1.73$, and $1.98 < z < 2.73$ for ERIS). We selected targets at high Galactic latitude ($b > 20°$) and near a star that was bright enough to drive the AO system. We selected five targets, three of which (J0812+2007, J0950+4329, and J1318−0136) are in the LBT sample described in Sect. 3.1.1. Table 3 summarizes the obtained observations, which are described in the next sections.

3.3.1. Keck/OSIRIS IFU spectra

Keck spectra were obtained on February 8, 2023, using a pixel scale of 50 mas. In all cases, the AO module was driven by a laser guide star (LGS) and a nearby natural tip-tilt (TT) star to correct for the low orders. The positions of the two components in J0812+2007 and J0950+4329 were known before the observations from the *Gaia* catalog and the LBT observations. The knowledge of the position angle in these two cases allowed us to use a smaller field of view ($0.8'' \times 3.2''$) with a broader wavelength coverage (OSIRIS filters Hbb and Jbb, respectively). In contrast, J1048+4541 and J1103+2348 are isolated sources in the *Gaia* database, and the position of the companion was not known before the observations. As a consequence, we used a narrower wavelength coverage (Hn3 in both cases) to have a larger field of view ($1.6'' \times 3.2''$) that is matched the expected separations below $0.7''$ well. In addition to the science targets, we also observed a standard star of spectral type A for telluric calibration on each night. All data cubes were assembled and reduced using the standard OSIRIS pipeline (Lockhart et al. 2019; see Ciurlo et al. 2023 for more details). Figure 4 shows the images of the observed systems (left panels) and the spectra (right panels) obtained via a weighted sum in the shown apertures.

All the systems show two point-like unresolved sources (see Fig. 4). J0812+2007 is constituted by an AGN, revealed by the broad Hα line, and a second object characterized by a featureless continuum. The most probable interpretation for the latter is that this is a star, which is expected in about 30% of the systems (Mannucci et al. 2022). Both components of J0950+4320 show QSO spectra, characterized by broad Hβ and Hγ and bright [OIII]4959,5007 lines. The two spectra become virtually identical by applying a small correction for dust extinction to component A for $A_V = 0.4$, and a normalization factor of 2.65. The similarity of the spectra and the luminosity of the object (see Fig. 3) suggest that this is a lensed QSO, in which the different dust extinction is produced by the different light paths for the two images. The lensing galaxy is not detected, but this is compatible with the relatively low sensitivity of our spectra to extended and continuum-dominated objects close to two bright point sources. Both J1048+4541 and J1103+2348 are constituted by two components each, and all the spectra show bright, very broad Hα lines. The line profiles in each pair are very different, both in center and shapes. To quantify the difference, we fit a Gaussian line and a constant continuum to each broad emission line. The formal errors on both line center and FWHM are small, a few km s^{-1}, but the real uncertainties due to the non-Gaussian profiles of the line and the partial coverage of some of the lines are larger. For this reason, we estimate typical uncertainties of ∼100−200 km s^{-1} on the centers and 200−500 km s^{-1} on the FWHM. The Hα central wavelengths of the two components of J1048+4541 differ by 500 ± 300 km s^{-1}, and the two lines have very different line widths, that is, $FWHM = 2500 \pm 200$ km s^{-1} for component A and $FWHM = 5300 \pm 500$ km s^{-1} for component B. The significance of the velocity offset is hampered by the lack of most of the blue part of the line of component B, while the difference in line width is highly significant. The two components of J1103+2348 have similar line widths ($FWHM = 2950 \pm 400$ km s^{-1} in both cases), but the central wavelengths are offset by 430 ± 200 km s^{-1}. In addition, the line shapes are very different and have opposite asymmetries. These differences are not compatible with two lensed images of one variable source, but they are compatible with different delays: In both cases, the expected time delay between the two components is a few days at most, while the luminosities of the objects imply BLR sizes of hundreds of days (Bentz et al. 2013).

3.3.2. VLT/ERIS IFU spectra

J1318−0136 was observed on April 14, 2023, with ERIS on the VLT during the first run of the INAF guaranteed-time observations (GTO) time on this instrument, using a LGS and a nearby TT star. We used the SPIFFIER IFU spectrograph (George et al. 2016), which is an upgrade of the SPIFFI spectrograph (Eisenhauer et al. 2003) and covers a field of view of

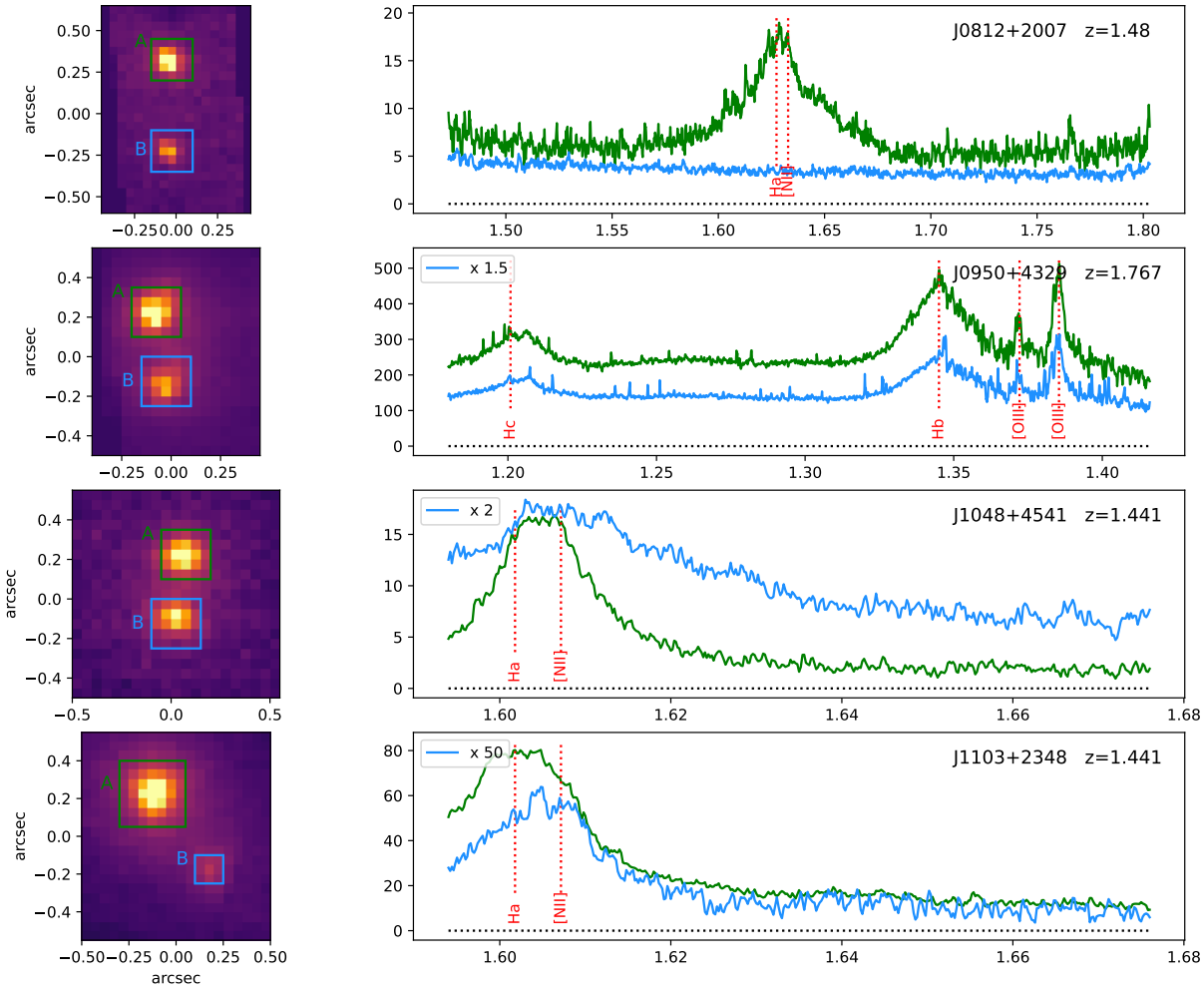

Fig. 4. Hα emission line maps (left) and spectra (right) of the systems observed with OSIRIS (target name and redshift reported in the right panels). The line maps are oriented with north at the top and west to the right. The spectra shown in the right panels have been extracted over the squared apertures marked on the left panes (with the same color-coding). Each component of the systems is labeled as in Table 4. To optimize the visualization, some of the spectra have been multiplied by arbitrary factors, which are reported in the top left corner of the corresponding panels. The vertical dotted lines show the position of the main expected emission lines.

3.2″ × 3.2″ with 50 mas sampling. We integrated for 30 min using the H-band grating, which provides a spectral resolution of $R \sim 5200$ in the wavelength range between 1.45 µm and 1.85 µm. The data were reduced with the automatic pipeline[5]. The PSF has an $FWHM = 120$ mas, limited by the 50 mas spaxel scale.

In Fig. 5 we show an image of the system that presents two well-separated components at a separation of 0.27″, and the spectra of the two sources that were extracted using circular apertures with a diameter of 200 mas after a second-pass background in each spectral plane of the cube was removed. The bright Hα emission line centered at 1.6375 µm corresponds to redshift $z = 1.495$ and agrees well with the tabulated value of $z = 1.486$ obtained from rest-frame UV lines, clearly revealing the AGN nature of the brightest component A. In contrast, component B shows no emission lines and a few absorption features, revealing that it is a foreground star.

In conclusion, Keck and VLT spectroscopy has allowed us to reliably classify five GMP-selected QSOs: two are AGN/star projection, one is a lensed systems, and two are dual AGNs, with the properties reported in Table 4. In the next section, these classifications are compared with those obtained from the near-IR colors (Sect. 3.1) and with all spectra (Sect. 3.2).

3.4. Comparison between different classifications

The three independent classification based on near-IR colors, integrated spectra, and spatially resolved spectroscopy are compared in Table 5. The agreement between all available classifications appears to be excellent.

- J0812–0040 and J1510+5959 are classified as AGN/star associations by the available methods, that is, colors and integrated spectra.
- J0812+2007 is an AGN/star systems based on the Keck spectrum, in agreement with the integrated spectrum. The large error on its $H - K_s$ color does not allow us to obtain a definite classification from the colors, which nevertheless are compatible with the presence of a star.
- The classification of J0950+4329 as a lensed system was obtained from the color-magnitude diagram and is confirmed by the IFU spectrum.
- J1048+4541 and J1103+2348 are classified as dual AGN systems by both the integrated and the IFU spectra.

[5] https://www.eso.org/sci/software/pipelines/eris/eris-pipe-recipes.html

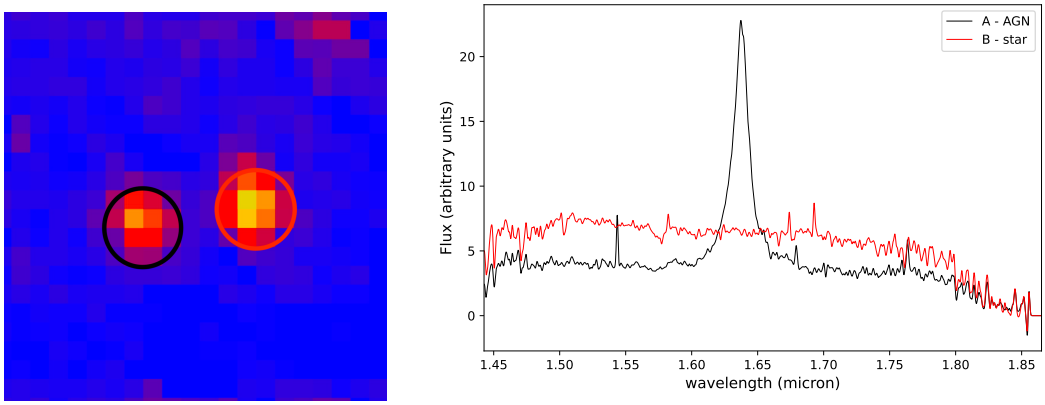

Fig. 5. Image (left) and uncalibrated H-band spectra (right) of J1318−0136, obtained with VLT/ERIS. The image has a size of 1″ × 1″ and is oriented with north at the top and west to the right. The spectra on the right are extracted using the circular apertures of 200 mas diameter shown in the image. The bright emission line is the Hα of AGN, while the other component only shows absorption features.

Table 4. Summary of the results from VLT/ERIS and Keck/OSIRIS observations.

Target	Class [a]	Separation [b]		Lines	Center	*FWHM*	Redshift
		(arcsec)	(kpc)		(μm)	(km s^{-1})	
J0812+2007A	AGN	0.61	–	Hα	1.628	7400	1.481
J0812+2007B	Star			–	–	–	–
J0950+4329A	Lensed AGN	0.37	2.0	Hα+[NII]	1.345	4890	1.767
J0950+4329B				Hα+[NII]	1.345	4830	1.767
J1048+4541A	Dual AGN	0.30	2.6	Hβ	1.605	2520	1.446
J1048+4541B				Hβ	1.608	5330	1.450
J1103+2348A	Dual AGN	0.52	4.4	Hα+[NII]	1.602	2990	1.442
J1103+2348B				Hα+[NII]	1.605	2960	1.445
J1318−0136A	AGN	0.27	–	Hα	1.637	2990	1.495
J1318−0136B	Star			–	–	–	–

Notes. [a]Most probable classification. [b]Projected angular and linear distances from the brightest object.

– The spectrum of J0732+3533 does not show any stellar contribution, while the colors are compatible with both AGN/AGN and AGN/star systems.
– J1318–0136 is classified as an AGN/star alignment based on its near-IR colors, but the spectrum is of low quality and cannot be used for a reliable classification. The ERIS spectra confirm this classification.
– Finally, J0927+3512 is a peculiar system. While the LAMOST survey classifies this object as a secure QSO at z = 1.149, our spectrum does not show any clear emission line, and the MgIIλ2800 line expected at 6017 Å is not detected. Thus, the presence of an AGN in this system is not secure, nor is its redshift. Both components show very blue $H - K_s$ colors, which indicate a classification as a star pair when they are combined with the high apparent magnitude ($H < 15.5$). In contrast, its spectrum is not a clear superposition of two stars. The nature of this system remains uncertain.

To summarize, while spatially resolved spectra are the ultimate tool for securing a classification, the combination of integrated spectra, magnitudes, and colors is a useful method for classifyig GMP systems with relatively high confidence.

Table 5. System classification.

Target	Classification method		
	Integr. [a] spectrum	Colors [b]	Resolved [c] spectrum
J0732+3533	AGN	Unclass.	–
J0812−0040	AGN+star	AGN+star	–
J0812+2007	AGN+star	Unclass.	AGN+star
J0927+3512	Unclass.	Stars?	–
J0950+4329	AGN	Lensed AGN	Lensed AGN
J1048+4541	AGN	–	Dual AGN
J1103+2348	AGN	–	Dual AGN
J1318−0136	Unclass.	AGN+star	AGN+star
J1510+5959	AGN+star	AGN+star	–

Notes. Method used: [a]deconvolution of integrated archival spectra. [b]Near-IR colors from LBT images. [c]IFU spectroscopy with Keck/OSIRIS or VLT/ERIS.

4. Discussion and conclusions

In Sect. 2 we have shown that the GMP method has a simple and well-defined selection function in terms of the separation of the sources and their luminosity ratios. This is a key feature for comparing the properties of the discovered dual and lensed systems with the theoretical predictions, and for testing some of the aspects of the models of hierarchical formation of galaxies and SMBH for the first time.

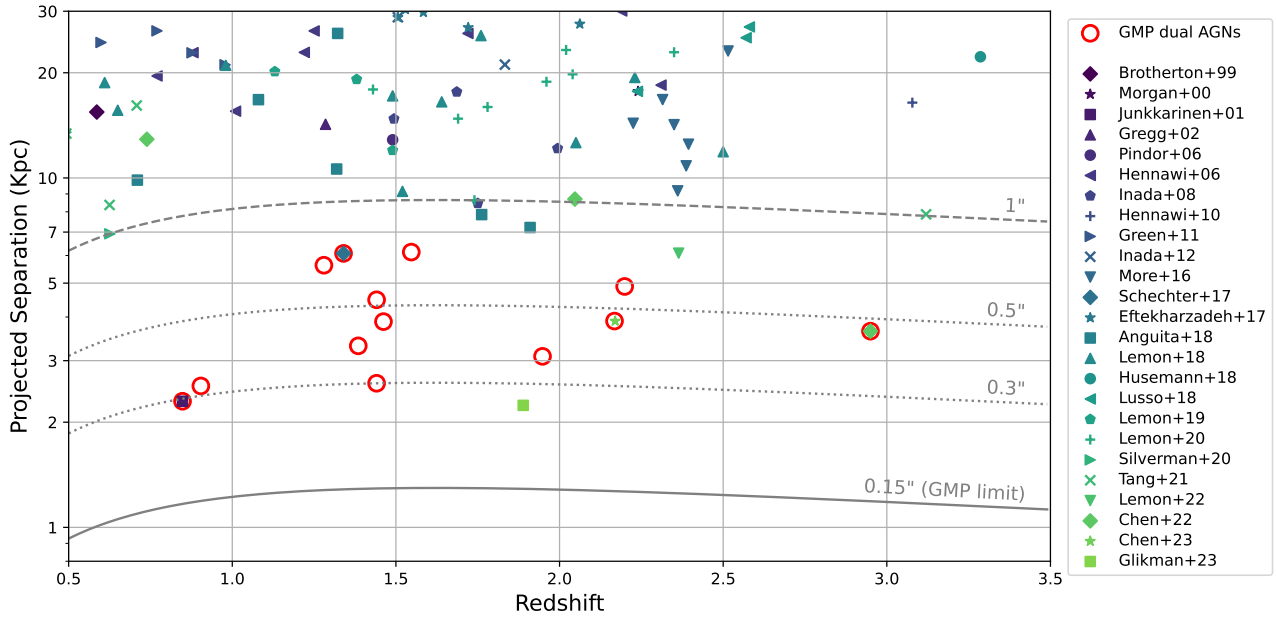

Fig. 6. Projected separation vs. redshift of all the spectroscopically confirmed dual AGNs with separations smaller than 30 kpc. Literature data are from Brotherton et al. (1999), Morgan et al. (2000), Junkkarinen et al. (2001), Gregg et al. (2002), Pindor et al. (2006), Hennawi et al. (2006, 2010), Inada et al. (2008, 2012), Green et al. (2011), More et al. (2016), Eftekharzadeh et al. (2017), Schechter et al. (2017), Husemann et al. (2018), Lusso et al. (2018), Lemon et al. (2018, 2019, 2020, 2022), Silverman et al. (2020), Tang et al. (2021), Chen et al. (2022, 2023b), and Glikman et al. (2023). The red circles show the GMP systems, empty circles show the dual AGNs that were originally selected with this techniques and were described in Mannucci et al. (2022), Ciurlo et al. (2023), Scialpi et al. (2023), and this work.

Based on integrated spectra and AO-assisted observations at the VLT, Keck, and LBT, we showed that a combination of integrated spectra and spatially resolved near-IR luminosity and colors can provide indications of the nature of these systems as dual AGNs, lensed QSOs, or an AGN/star alignment.

Mannucci et al. (2022), Ciurlo et al. (2023), Scialpi et al. (2023), and this work presented samples of dual AGNs selected with the GMP method and classified with resolved spectroscopy. In total, 22 GMP systems were classified, and we obtained ten dual AGNs, five lensed systems (including the system classified as a lens by Li et al. 2023), and seven AGN/star associations. One of these systems and three more GMP candidates have previously been identified using other techniques. Junkkarinen et al. (2001) reported the serendipitous discovery with the HST of a very compact dual system at $z \sim 0.84$, which consists of two components separated by $\sim$0.3″. Schechter et al. (2017) identified a dual system at $z = 1.34$ and $\delta = 0.71''$ by spatial deconvolution of ground-based images of AGNs selected to have red WISE $W1-W2$ colors. Chen et al. (2022) identified several multiple AGN candidates by searching for SDSS systems associated with more than one *Gaia* object within a few arcseconds. One of these systems was spectroscopically confirmed to be a dual AGN at $z = 2.95$ and with a separation of 0.46″ (Mannucci et al. 2022). As shown in Fig. 1, this technique becomes very inefficient at $\delta < 0.5''$, but can sporadically provide targets down to $\delta \sim 0.3''$. Finally, Chen et al. (2023b) presented a detail analysis of one target at $z = 2.17$ with a separation of $\delta = 0.46''$ selected using varstrometry, which is the *Gaia* astrometric additional jitter due to the unrelated variation of the two AGNs.

Figure 6 shows the distribution in redshift and projected separations of all the known dual AGNs with separations smaller than 30 kpc. It is evident that all the 14 systems with separations smaller than 7 kpc are GMP-selected systems, and 9 of these are only detected with this method. The only exceptions are the complex system discovered by Lemon et al. (2022) at $z = 2.36$, which is a lensed system with six components with large separations (up to $\sim$4″), possibly attributable to a dual systems with a separation of $\sim$0.7″, a very interesting but uncertain and peculiar system, and the dual system at $z = 1.889$ and $\delta = 2.2$ kpc that was serendipitously discovered by Glikman et al. (2023), whose luminosity ratio between the components is too high for it to be selected with GMP (see Fig. 2).

In conclusion, the GMP method appears to be the best-suited technique to provide a large sample of high-redshift dual AGNs residing in the same host galaxies. We are currently in the process of confirming more systems with AO spectroscopic observations, in particular, with VLT/MUSE, VLT/ERIS, and Keck/OSIRIS, to obtain a sample that is large enough to test the prediction of models of galaxy formation and evolution.

We summarize our results below.

- We tested the performances of the GMP selection using dense stellar fields with numerous projected pairs at low separations. This allowed us to estimate the level of contamination (false positives) as a function of the selecting parameter `FMP` (Fig. 1, left) and the selection efficiency as a function of separation δ (Fig. 1, left) and source magnitudes (Fig. 2). The results show that low levels of contamination and high selection efficiency can be obtained for $\delta > 0.15''$ and $G < 20.5$.
- AO-assisted imaging in the H and K_s band with SOUL/LUCI at LBT of seven GMP-selected systems allowed us to resolve all of them into multiple components, to measure the $H - K_s$ of all the sources, and to develop a new color-based method for identifying the most probable nature of the GMP-selected systems (Fig. 3).
- We reproduced the integrated ground-based spectra of the nine systems of this sample with a combination of an AGN template with a foreground star. Four of these nine systems are well reproduced by a simple AGN spectrum (Fig. A.1), three show clear evidence for the presence of an AGN and a star (Fig. A.2), and two remain unclassified (Fig. A.3).

– We presented the spatially resolved spectra of five systems with Keck/OSIRIS (Fig. 4) and VLT/ERIS (Fig. 5). These spectra allowed us to discover two dual systems with separations of 0.30″ and 0.52″, a very compact lensed system (separation 0.25″), and two AGN/star associations.
– By comparing the various classification methods, we showed that the combined analysis of resolved colors and integrated spectra can provide reliable classifications of the systems in most cases.
– Figure 6 shows all the confirmed dual AGNs at $z > 0.5$ and separations smaller than 30 kpc. Fourteen of the 15 systems with separations below ∼7 kpc are GMP systems, and 10 of them are originally selected with this method. In other words, since its introduction (Mannucci et al. 2022), this techniques has already allowed us to triple the confirmed systems at small separations. This result shows that the GMP technique is an important step forward in sampling the dual AGNs hosted by the same galaxy and testing the predictions of the models at $\delta < 7$ kpc.

Acknowledgements. We are grateful to the teams of VLT/ERIS and LBT/SOUL for proving us with excellent instruments for this project, and to the staffs of Keck, VLT and LBT for superb support during the observations; we acknowledge the use of 2 h of INAF discretionary time at LBT. We thank Stefano Cristiani, Andrea Grazian, and Robert Smith for assistance with ground-based, integrated spectra. We acknowledge financial contribution from INAF Large Grant "Dual and binary supermassive black holes in the multi-messenger era: from galaxy mergers to gravitational waves" (Bando Ricerca Fondamentale INAF 2022), and from the French National Research Agency (grant ANR-21-CE31-0026, project MBH_waves). Based on observations collected at the European Southern Observatory under ESO programme 111.24QJ.001. This work has made use of data from the European Space Agency (ESA) mission *Gaia* (https://www.cosmos.esa.int/gaia), processed by the *Gaia* Data Processing and Analysis Consortium (DPAC, https://www.cosmos.esa.int/web/gaia/dpac/consortium). Funding for the DPAC has been provided by national institutions, in particular the institutions participating in the *Gaia* Multilateral Agreement. Funding for the Sloan Digital Sky Survey (SDSS) has been provided by the Alfred P. Sloan Foundation, the Participating Institutions, the National Aeronautics and Space Administration, the National Science Foundation, the US Department of Energy, the Japanese Monbukagakusho, and the Max Planck Society. The SDSS website is http://www.sdss.org. The SDSS is managed by the Astrophysical Research Consortium (ARC) for the Participating Institutions. The Participating Institutions are The University of Chicago, Fermilab, the Institute for Advanced Study, the Japan Participation Group, The Johns Hopkins University, Los Alamos National Laboratory, the Max-Planck-Institute for Astronomy (MPIA), the Max-Planck-Institute for Astrophysics (MPA), New Mexico State University, University of Pittsburgh, Princeton University, the United States Naval Observatory, and the University of Washington.

References

Amaro-Seoane, P., Andrews, J., Arca Sedda, M., et al. 2023, Liv. Rev. Relat., 26, 2
Arzoumanian, Z., Baker, P. T., Brazier, A., et al. 2018, ApJ, 859, 47
Bentz, M. C., Denney, K. D., Grier, C. J., et al. 2013, ApJ, 767, 149
Brotherton, M. S., Gregg, M. D., Becker, R. H., et al. 1999, ApJ, 514, L61
Capelo, P. R., Dotti, M., Volonteri, M., et al. 2017, MNRAS, 469, 4437
Chen, Y. C. 2021, ArXiv e-prints [arXiv:2109.06881]
Chen, Y.-C., Hwang, H.-C., Shen, Y., et al. 2022, ApJ, 925, 162
Chen, N., Di Matteo, T., Ni, Y., et al. 2023a, MNRAS, 522, 1895
Chen, Y.-C., Liu, X., Foord, A., et al. 2023b, Nature, 616, 45
Ciurlo, A., Mannucci, F., Yeh, S., et al. 2023, A&A, 671, L4
Civano, F., Marchesi, S., Comastri, A., et al. 2016, ApJ, 819, 62
Covey, K. R., Ivezić, Ž., Schlegel, D., et al. 2007, AJ, 134, 2398
Croom, S. M., Smith, R. J., Boyle, B. J., et al. 2004, MNRAS, 349, 1397
Croom, S. M., Richards, G. T., Shanks, T., et al. 2009, MNRAS, 399, 1755
DeGraf, C., Chen, N., Ni, Y., et al. 2023, MNRAS, in press, https://doi.org/10.1093/mnras/stad3084
De Rosa, A., Vignali, C., Bogdanović, T., et al. 2019, New Astron. Rev., 86
Dong-Páez, C. A., Volonteri, M., Beckmann, R. S., et al. 2023, A&A, 673, A120
Eftekharzadeh, S., Myers, A. D., Hennawi, J. F., et al. 2017, MNRAS, 468, 77
Eisenhauer, F., Abuter, R., Bickert, K., et al. 2003, SPIE Conf. Ser., 4841, 1548
Euclid Collaboration (Scaramella, R., et al.) 2022, A&A, 662, A112
Flesch, E. W. 2021, ArXiv e-prints [arXiv:2105.12985]
Gaia Collaboration (Prusti, T., et al.) 2016, A&A, 595, A1
Gaia Collaboration (Vallenari, A., et al.) 2023, A&A, 674, A1
George, E. M., Gräff, D., Feuchtgruber, H., et al. 2016, SPIE Conf. Ser., 9908, 99080G
Girardi, L., Groenewegen, M. A. T., Hatziminaoglou, E., & da Costa, L. 2005, A&A, 436, 895
Glikman, E., Langgin, R., Johnstone, M. A., et al. 2023, ApJ, 951, L18
Green, P. J., Myers, A. D., Barkhouse, W. A., et al. 2011, ApJ, 743, 81
Gregg, M. D., Becker, R. H., White, R. L., et al. 2002, ApJ, 573, L85
Hennawi, J. F., Strauss, M. A., Oguri, M., et al. 2006, AJ, 131, 1
Hennawi, J. F., Myers, A. D., Shen, Y., et al. 2010, ApJ, 719, 1672
Husemann, B., Worseck, G., Arrigoni Battaia, F., & Shanks, T. 2018, A&A, 610, L7
Hwang, H.-C., Shen, Y., Zakamska, N., & Liu, X. 2020, ApJ, 888, 73
Inada, N., Oguri, M., Becker, R. H., et al. 2008, AJ, 135, 496
Inada, N., Oguri, M., Shin, M.-S., et al. 2012, AJ, 143, 119
Junkkarinen, V., Shields, G. A., Beaver, E. A., et al. 2001, ApJ, 549, L155
Lemon, C. A., Auger, M. W., McMahon, R. G., & Ostrovski, F. 2018, MNRAS, 479, 5060
Lemon, C. A., Auger, M. W., & McMahon, R. G. 2019, MNRAS, 483, 4242
Lemon, C., Auger, M. W., McMahon, R., et al. 2020, MNRAS, 494, 3491
Lemon, C., Millon, M., Sluse, D., et al. 2022, A&A, 657, A113
Li, J., Liu, X., Shen, Y., et al. 2023, ApJ, 955, L16
Lockhart, K. E., Do, T., Larkin, J. E., et al. 2019, AJ, 157, 75
Lusso, E., Fumagalli, M., Rafelski, M., et al. 2018, ApJ, 860, 41
Lyke, B. W., Higley, A. N., McLane, J. N., et al. 2020, ApJS, 250, 8
Mandel, H., Seifert, W., Lenzen, R., et al. 2007, Astron. Nachr., 328, 626
Mannucci, F., Pancino, E., Belfiore, F., et al. 2022, Nat. Astron., 6, 1185
More, A., Oguri, M., Kayo, I., et al. 2016, MNRAS, 456, 1595
Morgan, N. D., Burley, G., Costa, E., et al. 2000, AJ, 119, 1083
Pindor, B., Eisenstein, D. J., Gregg, M. D., et al. 2006, AJ, 131, 41
Pinna, E., Esposito, S., Hinz, P., et al. 2016, SPIE Conf. Ser., 9909, 99093V
Pinna, E., Rossi, F., Puglisi, A., et al. 2021, ArXiv e-prints [arXiv:2101.07091]
Piotto, G., Milone, A. P., Bedin, L. R., et al. 2015, AJ, 149, 91
Rosas-Guevara, Y. M., Bower, R. G., McAlpine, S., Bonoli, S., & Tissera, P. B. 2019, MNRAS, 483, 2712
Schechter, P. L., Morgan, N. D., Chehade, B., et al. 2017, AJ, 153, 219
Scialpi, M., Mannucci, F., Marconcini, C., et al. 2023, A&A, submitted [arXiv:2305.11850]
Shen, Y., Hwang, H.-C., Zakamska, N., & Liu, X. 2019, ApJ, 885, L4
Shen, Y., Hwang, H.-C., Oguri, M., et al. 2023, ApJ, 943, 38
Silverman, J. D., Tang, S., Lee, K.-G., et al. 2020, ApJ, 899, 154
Simioni, M., Bedin, L. R., Aparicio, A., et al. 2018, MNRAS, 476, 271
Skrutskie, M. F., Cutri, R. M., Stiening, R., et al. 2006, AJ, 131, 1163
Steinborn, L. K., Dolag, K., Comerford, J. M., et al. 2016, MNRAS, 458, 1013
Tang, S., Silverman, J. D., Ding, X., et al. 2021, ApJ, 922, 83
Temple, M. J., Hewett, P. C., & Banerji, M. 2021, MNRAS, 508, 737
Tremmel, M., Karcher, M., Governato, F., et al. 2017, MNRAS, 470, 1121
Vanden Berk, D. E., Richards, G. T., Bauer, A., et al. 2001, AJ, 122, 549
Vanhollebeke, E., Groenewegen, M. A. T., & Girardi, L. 2009, A&A, 498, 95
Volonteri, M., Pfister, H., Beckmann, R., et al. 2022, MNRAS, 514, 640
Yao, S., Wu, X.-B., Ai, Y. L., et al. 2019, ApJS, 240, 6

Appendix A: Results of the spectral deconvolution

Table A.1. Best-fit parameters of the spectral deconvolution.

Target	z_{fit}	$E_{(B-V)}$	$G_{P,fit}$	$G_{S,fit}$	Star type	V_* [km/s]
J0732+3533	3.0529	0.0698				
J0812-0040	1.9147	0.0004	20.36	20.39	G0	+286
J0812+2007	1.4865	0.0358	20.16	21.46	G2	+57
J0927+33512	1.1605	0.0000				
J0950+4329	1.7700	0.1389				
J1048+4541	1.4432	0.0449				
J1103+2348	1.4384	0.1003				
J1318-0136	1.4881	0.1498				
J1510+5959	2.0212	0.0039	20.34	20.99	G3	-210

Notes. Best-fit parameters for the deconvolved sources. From left to right: Target ID, spectroscopic redshift (z_{fit}), and extinction ($E_{(B-V)}$) of the best-fitting QSO template. When an object is reproduced by an AGN plus a star, we report the G-band magnitude of the primary and secondary objects (($G_{P,fit}$) and $G_{S,fit}$, respectively), the spectral type of the best-fitting star, and its radial velocity (V_*).

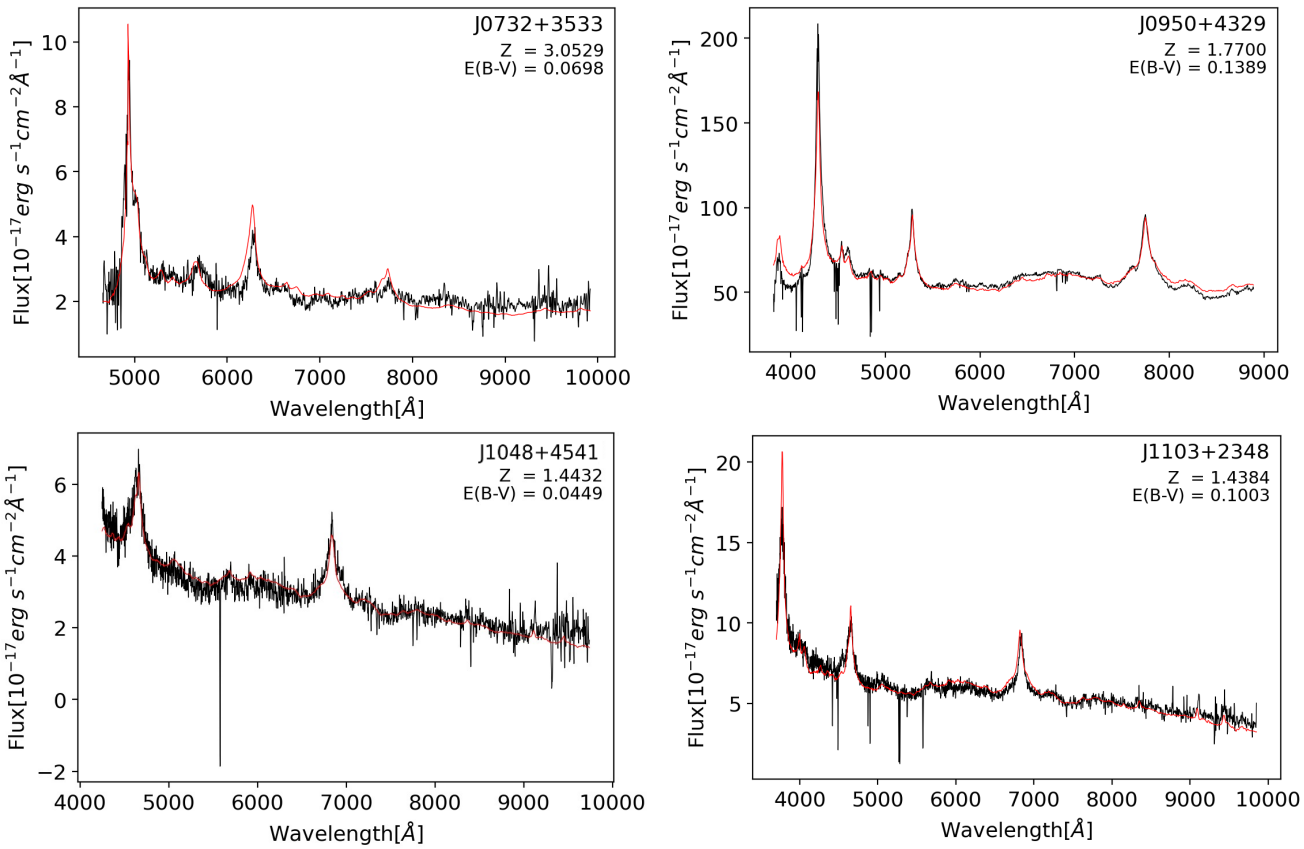

Fig. A.1. Spectral deconvolution of the objects that are best reproduced by an AGN spectrum. The observed spectrum is shown in black, and the best fit is plotted in red. Each panel reports the target ID and the best-fitting redshift and degree of dust extinction.

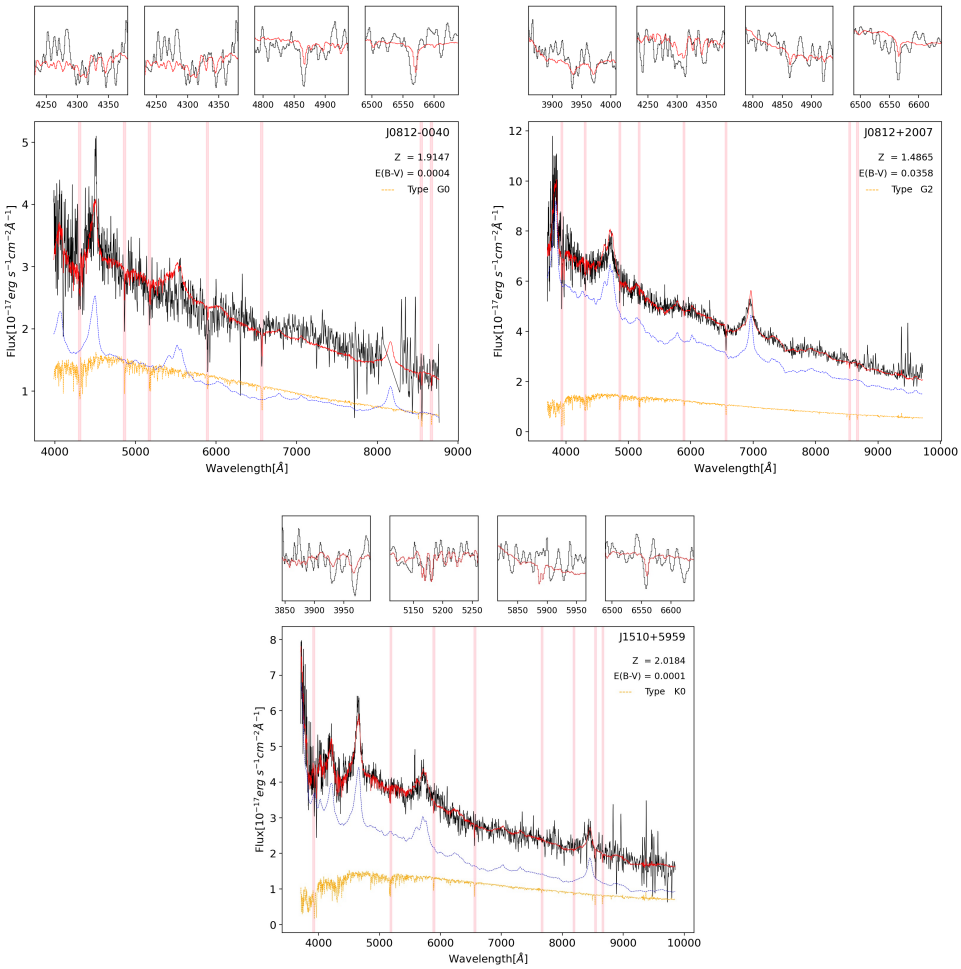

Fig. A.2. Spectral deconvolution of the systems that are best reproduced by a combination of an AGN and a star. The observed spectra are shown in black, the best fit is plotted in red, the QSO is shown in blue, and the stellar component is shown in orange, with vertical red stripes around the main stellar absorption features of the best-fitting stellar type. The four small panels above the main panels are enlargements of the main absorption features of the stellar companion.

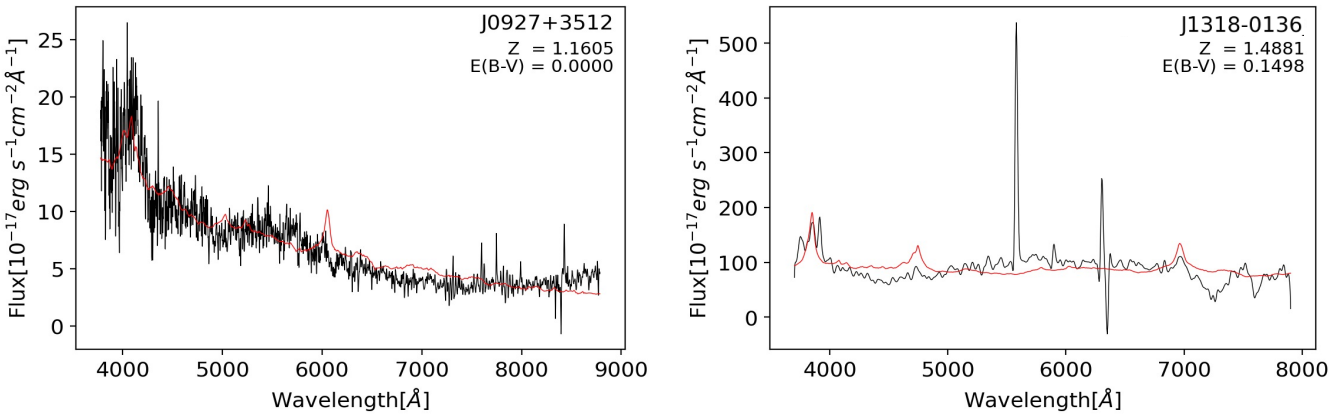

Fig. A.3. Spectral deconvolution of the unclassified objects, i.e., the systems whose spectra are not well reproduced from an AGN or from an AGN plus a star.